Journal of Theoretical and Applied Mechanics, Sofia, Vol.XX (20XX) pp. 1-20
FLUID MECHANICS

EFFECTS OF MAGNETIC FIELD ON HEAT AND MASS TRANSFER IN PULSATILE FLOW OF BLOOD UNDER STENOTIC CONDITION

SUBRATA MUKHOPADHYAY[1], MANI SHANKAR MANDAL[2*],
SWATI MUKHOPADHYAY[3]

[1]*Department of Mathematics, Acharya P.C. Roy Govt. College, Siliguri, W.B., India*
[2]*Department of Mathematics, G.G.D.C at Kalna-I, Purba Bardhaman-713405, W.B., India*
[3]*Department of Mathematics, The University of Burdwan, Burdwan-713104, W.B., India*

[Received: 8 May 2021

ABSTRACT: A mathematical model is developed in the present study to investigate the heat and mass transfer phenomena in blood flow under stenotic condition. The non-Newtonian Carreau fluid model is used to characterize the streaming blood. The nonlinear governing equations are solved numerically by employing a finite difference scheme along with suitable initial and boundary conditions under the action of applied magnetic field. Various significant hemodynamic parameters are examined for additional qualitative insight of the flow-field, temperature-field and concentration-field over the entire flow regime with the help of the numerical results obtained in this study. Comparisons are made with available results in open literature and are found in good agreement between these two results.

KEY WORDS: Heat and mass transfer, Non-Newtonian fluid, Magnetic field, Finite-difference.

1 INTRODUCTION

Heat and mass transfer phenomena in constricted channels have significant practical implications in engineering fields and Biorheology. The motion of an electrically conducting fluid across a magnetic field induces current, which affects the fluid flow. In fact the propagating field is influenced by Lorentz force. Understanding the physics of magnetohydrodynamic (MHD) flow, prediction of flow separation region

*Corresponding author e-mail: manimath@yahoo.com

and flow bifurcation phenomenon is crucial in many engineering flow devices. Beside, the study of MHD blood flow in arteries is of paramount physical interest due to its significant clinical implications. For instance, studies in magnetic drug targeting to the whole body and the development of magnetic devices for cell separation [1, 2]. Several research works revealed that the application of a uniform transverse magnetic field alters the hemodynamic parameters and temperature of streaming blood.

Fluid flow separation is a fundamental problem in fluid mechanics. Separation of flow is an undesirable phenomenon in engineering applications [3, 4]. Flow separation causes energy loss, slow pressure recovery, increase of thickness of boundary layer developed over a surface etc. Performance of fluid flow devices depends significantly on the control of flow separation phenomenon and instability of flow [5]. Control of flow quantities with the application of electromagnetic forces is therefore an attractive research area to fluid mechanists.

The steady flow of an electrically conducting fluid in a channel in presence of a uniform transverse magnetic field was studied by many researchers [6–8]. The velocity of flowing blood decreases significantly when the Hartmann number is increased substantially [9]. Pulsatile flow of blood through a two-dimensional stenosed channel was investigated by [10]. They used a non-Newtonian viscosity model for blood and assumed the flow field to be axisymmetric. Bandyopadhyay and Layek [11] studied the effect of magnetic field on pulsatile flow of a Newtonian fluid through a constricted channel. In their study it was revealed that the regions of flow separation could be controlled with the application of suitable magnetic field.

None of these studies has considered the heat and mass transfer phenomenon. Therefore a sincere attempt is taken in the present study to analyze the pulsatile flow of an electrically conducting non-Newtonian fluid (modeled as blood) through a constricted channel in presence of magnetic field. The aim of the present study is to report the effect of magnetic field, applied in the transverse direction, on the flow field and heat and mass transfer along the channel wall. The induced magnetic field is neglected due to the low electrical conductivity of streaming blood.

2 Blood Viscosity Model

Most of the industrial fluids or biological fluids are non-Newtonian in nature. Human blood, flowing through small diameter arteries at low shear-rate shows deviation from Newtonian viscosity. Several experimental observations established that the viscosity of blood is a decreasing function of its shear rate and has asymptotic values for very low or very high shear rates. Several constitutive equations, representing this shear thinning behaviour, are found in literature.

The shear dependent Carreau viscosity model consists of four parameters and is

described as [12]

$$\mu^*(\dot{\gamma}^*) = \mu_\infty + (\mu_0 - \mu_\infty)(1 + \Lambda^{*2}\dot{\gamma}^*)^{(n-1)/2}, \tag{1}$$

where $\dot{\gamma}^*$ is the shear rate, μ_0 and μ_∞ are the asymptotic zero and infinite shear viscosities, $\Lambda^* \geq 0$ is a material constant that represents the degree of shear thinning. Values of these parameters for human blood, found in literature, are $\mu_0 = 0.056$ Pa s, $\mu_\infty = 0.00345$ Pa s, $\Lambda^* = 3.313$ s, $n = 0.3568$ [12].

3 Formulation of the Problem

3.1 Governing Equations

We consider the two-dimensional laminar pulsatile flow of an electrically conducting incompressible viscous non-Newtonian fluid with electrical conductivity σ and constant density ρflowing through an infinite rigid walled parallel plate channel having axisymmetric constrictions on both walls (a model of blood flow through a rigid artery with stenosis). Let x^*, y^*) be the Cartesian coordinate of a material point in the flow regime, where the x^*-axis is along the lower wall. Let u^*v^* be the velocity components along the x^*, y^* directions respectively. Let p^* be the pressure, T^* be the temperature and c^* be the concentration field of the fluid.

Consider a uniform magnetic field B_0 which is applied in the direction of y^*-axis. The magnetic permeability of the conducting medium is assumed to be constant.

Let us introduce the following non-dimensional variables:

$$\begin{aligned}
&x = \frac{x^*}{h}, && y = \frac{y^*}{h}, && u = \frac{u^*}{U_0}, && v = \frac{v^*}{U_0},\\
&p = \frac{p^*}{\rho U_0^2}, && t = \frac{t^*}{T}, && \theta = \frac{T^* - T_w^*}{T_\infty^* - T_w^*}, && c = \frac{c^* - c_w^*}{c_\infty^* - c_w^*},\\
&\mu = \frac{\mu^*}{\mu_\infty}, && \lambda = \frac{\mu_0}{\mu_\infty}, && \Lambda = \frac{\Lambda^* U_0}{h}, && \dot{\gamma} = \frac{\dot{\gamma}^* h}{U_0},
\end{aligned} \tag{2}$$

where h is the height of the non-constricted part of the channel, U_0 is the maximum flow velocity in the x-direction, T is the period of the flow pulsation, T_w^*, T_∞^* and c_w^*, c_∞^* be respectively the uniform temperature and concentration along the channel walls and at the inlet. The unsteady two dimensional Navier-Stokes' equations of motion of an electrically conducting incompressible non-Newtonian viscous fluid in presence of magnetic field may be written in dimensionless form as [13, 14]

$$\begin{aligned}
&St\frac{\partial u}{\partial t} + u\frac{\partial u}{\partial x} + v\frac{\partial u}{\partial y}\\
&\qquad = -\frac{\partial p}{\partial x} + \frac{1}{Re}\left[2\frac{\partial}{\partial x}\left(\mu\frac{\partial u}{\partial x}\right) + \frac{\partial}{\partial y}\left\{\mu\left(\frac{\partial u}{\partial y} + \frac{\partial v}{\partial x}\right)\right\}\right] - \frac{Ha^2}{Re}u
\end{aligned} \tag{3}$$

and

$$(4)\quad St\frac{\partial v}{\partial t}+u\frac{\partial v}{\partial x}+v\frac{\partial v}{\partial y}=-\frac{\partial p}{\partial y}+\frac{1}{Re}\left[2\frac{\partial}{\partial y}\left(\mu\frac{\partial v}{\partial y}\right)+\frac{\partial}{\partial x}\left\{\mu\left(\frac{\partial u}{\partial y}+\frac{\partial v}{\partial x}\right)\right\},\right]$$

where $St = h/(U_0T)$ is the Strouhal number, $Re = \rho U_0 h/\mu_\infty$ is the Reynolds number and $Ha = B_0\sqrt{(\sigma h)/(U_0\rho)}$ is the Hartmann number. The last term in equation (3) represents the Lorentz force, which is the electro-magnetic force acting on the flow field.

The continuity equation is

$$(5)\qquad \frac{\partial u}{\partial x}+\frac{\partial v}{\partial y}=0\,.$$

Heat and mass transfer phenomena in streaming blood are governed by the following two dimensionless equations [13–15]:

$$(6)\quad St\frac{\partial\theta}{\partial t}+u\frac{\partial\theta}{\partial x}+v\frac{\partial\theta}{\partial y}=\frac{1}{Pr\,Re}\left(\frac{\partial^2\theta}{\partial x^2}+\frac{\partial^2\theta}{\partial y^2}\right)+\frac{Ec}{Re}\mu\dot{\gamma}^2+Ha^2Ec\,u^2$$

and

$$(7)\quad St\frac{\partial c}{\partial t}+u\frac{\partial c}{\partial x}+v\frac{\partial c}{\partial y}=\frac{1}{Re\,Sc}\left(\frac{\partial^2 c}{\partial x^2}+\frac{\partial^2 c}{\partial y^2}\right)+\frac{Sr}{Re}\left(\frac{\partial^2\theta}{\partial x^2}+\frac{\partial^2\theta}{\partial y^2}\right).$$

Here, $Pr = \mu c_p/k$ is the Prandtl number, $Ec = (U_0^2)/(c_p(T_\infty^* - T_w^*))$ is the Eckert number, $Sc = \mu/(\rho D)$ is the Schmidt number, $Sr = \dfrac{\rho D k_T(T_\infty^* - T_w^*)}{\mu_\infty T_m^*(c_\infty^* - c_w^*)}$ is the Soret number; c_p, k, D, k_T, T_m^* being the specific heat at constant pressure, the thermal conductivity, the coefficient of diffusion, the thermal diffusion ratio and the mean temperature of the streaming blood respectively.

The dimensionless blood viscosity is obtained as

$$(8)\qquad \mu\left(\dot{\gamma}\right) = 1 + (\lambda - 1)\left\{1 + \Lambda^2\dot{\gamma}\right\}^{(n-1)/2}$$

with

$$(9)\qquad \dot{\gamma} = \left[2\left\{\left(\frac{\partial u}{\partial x}\right)^2 + \left(\frac{\partial v}{\partial y}\right)^2\right\} + \left(\frac{\partial u}{\partial y} + \frac{\partial v}{\partial x}\right)^2\right]^{1/2}.$$

3.2 GEOMETRY OF THE CHANNEL

The functions $f_1(x)$ and $f_2(x)$ that represent the geometry of the lower and upper walls respectively may be represented mathematically in dimensionless form as [7, 16]

$$f_1(x) = \delta_1 e^{-a_1(x-b_1)^2} \quad -\infty < x < \infty \tag{10}$$

and

$$f_2(x) = 1 - \delta_2 e^{-a_2(x-b_2)^2} \quad -\infty < x < \infty\,, \tag{11}$$

where δ_1, δ_2 represent the heights of the constrictions, a_1, a_2 represent the rate at which the boundary profiles change and b_1, b_2 denote their positions. In our study, these parameters are taken as $\delta_1 = \delta_2 = 0.3$, $a_1 = a_2 = 1$ and $b_1 = b_2 = 3$ (Fig. 1).

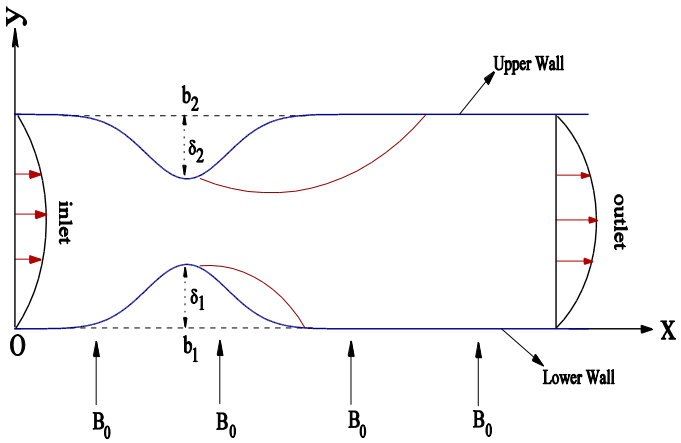

Fig. 1: Schematic diagram of the constricted channel.

4 STREAM FUNCTION-VORTICITY FORMULATION

Let us now introduce the dimensionless Stokes stream function $\psi(x, y, t)$ by

$$u = \frac{\partial \psi}{\partial y}\,, \qquad v = -\frac{\partial \psi}{\partial x} \tag{12}$$

and the corresponding vorticity function $\omega(x, y, t)$ by

$$\omega = \frac{\partial v}{\partial x} - \frac{\partial u}{\partial y}\,. \tag{13}$$

Cross-differentiation of the momentum equations (3) and (4), with use of (12) and (13), yields

$$St\frac{\partial\omega}{\partial t}+u\frac{\partial\omega}{\partial x}+v\frac{\partial\omega}{\partial y}=\frac{1}{Re}\Bigg[\mu\left(\frac{\partial^2\omega}{\partial x^2}+\frac{\partial^2\omega}{\partial y^2}\right)+2\left(\frac{\partial\mu}{\partial x}\frac{\partial\omega}{\partial x}+\frac{\partial\mu}{\partial y}\frac{\partial\omega}{\partial y}\right)+2\frac{\partial^2\mu}{\partial x\partial y}\left(\frac{\partial v}{\partial y}-\frac{\partial u}{\partial x}\right)+\left(\frac{\partial^2\mu}{\partial x^2}-\frac{\partial^2\mu}{\partial y^2}\right)\left(\frac{\partial u}{\partial y}+\frac{\partial v}{\partial x}\right)\Bigg]+\frac{Ha^2}{Re}\frac{\partial u}{\partial y}\,. \tag{14}$$

The mass conservation equation, with the use of (12) and (13), transforms to the Poisson equation given by

$$\frac{\partial^2\psi}{\partial x^2}+\frac{\partial^2\psi}{\partial y^2}=-\omega\,. \tag{15}$$

5 Initial and Boundary Conditions

The initial conditions for the velocity, temperature and concentration field were set as

$$u=y\left(1-y^2\right),\qquad v=0,\qquad \theta=y\left(1-y^2\right),\qquad c=y\left(1-y^2\right). \tag{16}$$

Though the initially chosen velocity, temperature or concentration profiles are not physiological, it is found that final results do not depend on these profiles. Further it is found that the results do not change significantly when the simulation runs for more than three time periods. Therefore, the simulation is carried out up to three time periods in all cases so that all transitional effects vanish within these time periods.

A time dependent non-dimensional pulsatile flow rate [17]

$$\mathrm{fr}(t)=0.4355+0.05\cos 2\pi t+0.25\sin 2\pi t-0.13\cos 4\pi t+0.13\sin 4\pi t-0.10\cos 6\pi t-0.02\sin 6\pi t-0.01\cos 8\pi t-0.03\sin 8\pi t \tag{17}$$

is assumed at the inlet cross section of the channel. Two parts of the physiological flow rate, systole and diastole, are included in this flow profile (Fig. 2). Here, $t=0.18$ and $t=0.45$ are respectively the times corresponding to the systolic and diastolic peak flows.

For the boundary condition at the outlet cross section of the channel, the flow is assumed to be fully developed i.e.

$$\frac{\partial\psi}{\partial x}=\frac{\partial\omega}{\partial x}=0\qquad\text{at}\quad x=L\,. \tag{18}$$

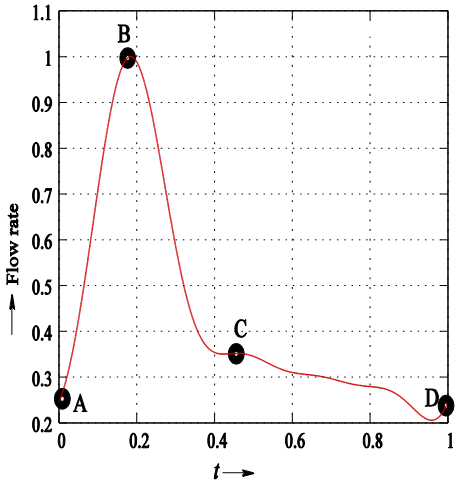

Fig. 2: Pulsatile flow rate.

The usual 'no slip' condition is imposed on the channel walls which gives

$$\frac{\partial \psi}{\partial x} = \frac{\partial \psi}{\partial y} = 0 \qquad \text{along } \; y = f_1(x) \; \text{ and } \; y = f_2(x)\,. \tag{19}$$

Now the mass flux across any cross-sections of the channel at any instant of time is

$$\text{fr}\,(t) = \int_{f_1(x)}^{f_2(x)} \frac{\partial \psi}{\partial y} dy\,.$$

This gives the value of the stream function ψ at the channel wall as

$$\psi\,(x, f_1\,(x)) = 0\,, \qquad \psi\,(x, f_2\,(x)) = \text{fr}\,(t)\,. \tag{20}$$

According to the choice of the non-dimensional variables θ and c,

$$\theta = 1\,, \qquad c = 1 \quad \text{at } \; x = 0 \tag{21}$$

and

$$\theta = 0\,, \qquad c = 0 \; \text{ along } \; y = f_1(x) \; \text{ and } \; y = f_2(x)\,. \tag{22}$$

At the outlet cross section of the channel, temperature and concentration gradient are assumed to be zero. Thus

$$\frac{\partial \theta}{\partial x} = 0\,, \qquad \frac{\partial c}{\partial x} = 0 \; \text{ at } \; x = L\,. \tag{23}$$

6 Coordinate Transformation

Let us choose a suitable coordinate system so that the constricted geometry transforms to a rectangular geometry in the transformed plane. For this, let us introduce the transformations [8]

$$\zeta = x\,, \qquad \eta = \frac{y - f_1(x)}{f_2(x) - f_1(x)}\,. \tag{24}$$

The vorticity transport equation (14) and the Poisson equation for pressure (15) is transformed in new coordinates (ζ, η) as

$$\begin{aligned} St\frac{\partial\omega}{\partial t} + u\Big(\frac{\partial\omega}{\partial\zeta} - \mathcal{B}\frac{\partial\omega}{\partial\eta}\Big) + v\mathcal{G}\frac{\partial\omega}{\partial\eta} = \frac{1}{Re}\Bigg[\mu\Big\{\frac{\partial^2\omega}{\partial\zeta^2} - 2\mathcal{B}\frac{\partial^2\omega}{\partial\zeta\partial\eta} \\ + (\mathcal{B}^2+\mathcal{G}^2)\frac{\partial^2\omega}{\partial\eta^2} - (\mathcal{A}-2\mathcal{B}\mathcal{H})\frac{\partial\omega}{\partial\eta}\Big\} + 2\Big\{\Big(\frac{\partial\mu}{\partial\zeta} - \mathcal{B}\frac{\partial\mu}{\partial\eta}\Big)\Big(\frac{\partial\omega}{\partial\zeta} - \mathcal{B}\frac{\partial\omega}{\partial\eta}\Big) + \mathcal{G}^2\frac{\partial\mu}{\partial\eta}\frac{\partial\omega}{\partial\eta}\Big\} \\ + 2\mathcal{G}\Big(\frac{\partial^2\mu}{\partial\zeta\partial\eta} - \mathcal{B}\frac{\partial^2\mu}{\partial\eta^2}\Big)\Big(\mathcal{G}\frac{\partial v}{\partial\eta} - \frac{\partial u}{\partial\zeta} + \mathcal{B}\frac{\partial u}{\partial\eta}\Big) + \Big\{\frac{\partial^2\mu}{\partial\zeta^2} - 2\mathcal{B}\frac{\partial^2\mu}{\partial\zeta\partial\eta} \\ + (\mathcal{B}^2 - \mathcal{G}^2)\frac{\partial^2\mu}{\partial\eta^2} - (\mathcal{A} - 2\mathcal{B}\mathcal{H})\frac{\partial\mu}{\partial\eta}\Big\}\Big(\mathcal{G}\frac{\partial u}{\partial\eta} + \frac{\partial v}{\partial\zeta} - \mathcal{B}\frac{\partial v}{\partial\eta}\Big)\Bigg] + \frac{Ha^2}{Re}\mathcal{G}\frac{\partial u}{\partial\eta} \end{aligned} \tag{25}$$

and

$$\frac{\partial^2\psi}{\partial\zeta^2} - 2\mathcal{B}\frac{\partial^2\psi}{\partial\zeta\partial\eta} + \left(\mathcal{B}^2 + \mathcal{G}^2\right)\frac{\partial^2\psi}{\partial\eta^2} - (\mathcal{A} - 2\mathcal{B}\mathcal{H})\frac{\partial\psi}{\partial\eta} = -\omega\,. \tag{26}$$

The transformed form of the heat and mass transport equations are given by

$$\begin{aligned} St\frac{\partial\theta}{\partial t} + u\Big(\frac{\partial\theta}{\partial\zeta} - \mathcal{B}\frac{\partial\theta}{\partial\eta}\Big) + v\mathcal{G}\frac{\partial\theta}{\partial\eta} = \frac{1}{Pr\,Re}\Bigg\{\frac{\partial^2\theta}{\partial\zeta^2} - 2\mathcal{B}\frac{\partial^2\theta}{\partial\zeta\partial\eta} \\ + (\mathcal{B}^2+\mathcal{G}^2)\frac{\partial^2\theta}{\partial\eta^2} - (\mathcal{A}-2\mathcal{B}\mathcal{H})\frac{\partial\theta}{\partial\eta}\Bigg\} + \frac{Ec}{Re}\mu\dot{\gamma}^2 + Ha^2 Ec\,u^2 \end{aligned} \tag{27}$$

and

$$\begin{aligned} St\frac{\partial c}{\partial t} + u\Big(\frac{\partial c}{\partial\zeta} - \mathcal{B}\frac{\partial c}{\partial\eta}\Big) + v\mathcal{G}\frac{\partial c}{\partial\eta} = \frac{1}{Re\,Sc}\Bigg\{\frac{\partial^2 c}{\partial\zeta^2} - 2\mathcal{B}\frac{\partial^2 c}{\partial\zeta\partial\eta} \\ + (\mathcal{B}^2+\mathcal{G}^2)\frac{\partial^2 c}{\partial\eta^2} - (\mathcal{A}-2\mathcal{B}\mathcal{H})\frac{\partial c}{\partial\eta}\Bigg\} + \frac{Sr}{Re}\Big\{\frac{\partial^2\theta}{\partial\zeta^2} - 2\mathcal{B}\frac{\partial^2\theta}{\partial\zeta\partial\eta} \\ + (\mathcal{B}^2+\mathcal{G}^2)\frac{\partial^2\theta}{\partial\eta^2} - (\mathcal{A}-2\mathcal{B}\mathcal{H})\frac{\partial\theta}{\partial\eta}\Big\}. \end{aligned} \tag{28}$$

The quantities $\mathcal{A}$, $\mathcal{B}$, $\mathcal{G}$ and $\mathcal{H}$ are defined by

$$\mathcal{A} = \frac{\eta f_2'' + (1-\eta) f_1''}{f_2 - f_1}, \qquad \mathcal{G} = \frac{1}{f_2 - f_1}, \tag{29}$$
$$\mathcal{B} = \frac{\eta f_2' + (1-\eta) f_1'}{f_2 - f_1}, \qquad \mathcal{H} = \frac{f_2' - f_1'}{f_2 - f_1}.$$

The boundary conditions along $y = f_1(x)$ and $y = f_2(x)$ are now on $\eta = 0$ and $\eta = 1$ line.

7 Numerical Method

A finite difference technique is employed over a uniformly spaced grid in the (ζ, η) plane to solve the governing non-linear equations [4]. All spatial derivatives in equations (25)–(28) are discretized by central difference approximations, while the time derivatives are discretized by forward difference approximation.

A uniformly spaced grid is generated by introducing the mesh points (ζ_i, η_j) where $\zeta_i = i\Delta\zeta$ and $\eta_j = j\Delta\eta$, where $\Delta\zeta$ and $\Delta\eta$ are respective increments of ζ and η. The finite difference representation of t is $t_k = k\Delta t$, Δt being the time increment.

Corresponding to each line $\zeta = \zeta_i$ in η-direction, a tri-diagonal system of algebraic equations is formed. Equation (26) is arranged as

$$A(j)\psi_{i,j-1}^{k+1} + B(j)\psi_{i,j}^{k+1} + C(j)\psi_{i,j+1}^{k+1} = D(j), \tag{30}$$

where the quantities $A(j)$, $B(j)$, $C(j)$ and $D(j)$ have following values:

$$A(j) = \frac{\mathcal{A} - 2\mathcal{B}\mathcal{H}}{2\Delta\eta} + \frac{\mathcal{B}^2 + \mathcal{G}^2}{(\Delta\eta)^2},$$
$$B(j) = -\frac{2}{(\Delta\zeta)^2} - \frac{2\left(\mathcal{B}^2 + \mathcal{G}^2\right)}{(\Delta\eta)^2},$$
$$C(j) = -\frac{\mathcal{A} - 2\mathcal{B}\mathcal{H}}{2\Delta\eta} + \frac{\mathcal{B}^2 + \mathcal{G}^2}{(\Delta\eta)^2},$$
$$D(j) = -\omega_{i,j}^k - \frac{\psi_{i+1,j}^k + \psi_{i-1,j}^k}{(\Delta\zeta)^2} + \mathcal{B}\frac{\psi_{i+1,j+1}^k - \psi_{i+1,j-1}^k - \psi_{i-1,j+1}^k + \psi_{i-1,j-1}^k}{2\Delta\zeta\Delta\eta}.$$

Thomas algorithm [18] is used to solve the tri-diagonal system of equations (30) with the known values of $A(j)$, $B(j)$, $C(j)$ and $D(j)$ at the k^{th}-time level and the value of ψ at the $(k+1)^{\text{th}}$-time level is obtained. Updated value of ψ gives u and v as

$$u = \mathcal{G}\frac{\partial\psi}{\partial\eta}, \qquad v = -\frac{\partial\psi}{\partial\zeta} + \mathcal{B}\frac{\partial\psi}{\partial\eta}. \tag{31}$$

Obtained values of u and v are used in the coupled equations (3) and (4) to solve the pressure field over the flow regime. For this, a zero pressure is assigned at the inlet cross-section.

Employing the no-slip boundary condition on (31) and then using the equation (26) a second order accurate formulae for wall vortices are obtained as

$$\begin{aligned} \omega(\zeta,0) &= -2\left(\mathcal{B}^2+\mathcal{G}^2\right)\frac{\psi(\zeta,\Delta\eta)-\psi(\zeta,0)}{(\Delta\eta)^2}, \\ \omega(\zeta,1) &= -2\left(\mathcal{B}^2+\mathcal{G}^2\right)\frac{\psi(\zeta,1-\Delta\eta)-\psi(\zeta,1)}{(\Delta\eta)^2}. \end{aligned} \tag{32}$$

These formulae involves a coupling between the vorticity at the boundary and the stream function in the domain.

The momentum equation (25) is now solved exactly in the same way as stated above. The discretized form of the momentum equation is given by

$$P(j)\,\omega_{i,j-1}^{k+1}+Q(j)\,\omega_{i,j}^{k+1}+R(j)\,\omega_{i,j+1}^{k+1}=S(j), \tag{33}$$

where the quantities $P(j)$, $Q(j)$, $R(j)$ and $S(j)$ are given by

$$\begin{aligned} P(j) &= -\frac{v\mathcal{G}-u\mathcal{B}}{2\Delta\eta}-\mu\frac{\mathcal{A}-2\mathcal{B}\mathcal{H}}{2Re\Delta\eta}-\frac{\mathcal{B}}{Re\Delta\eta}\left(\frac{\partial\mu}{\partial\zeta}-\mathcal{B}\frac{\partial\mu}{\partial\eta}\right)-\mu\frac{\mathcal{B}^2+\mathcal{G}^2}{Re(\Delta\eta)^2}, \\ Q(j) &= \frac{St}{\Delta t}+2\mu\frac{\mathcal{B}^2+\mathcal{G}^2}{Re(\Delta\eta)^2}, \\ R(j) &= \frac{v\mathcal{G}-u\mathcal{B}}{2\Delta\eta}+\mu\frac{\mathcal{A}-2\mathcal{B}\mathcal{H}}{2Re\Delta\eta}+\frac{\mathcal{B}}{Re\Delta\eta}\left(\frac{\partial\mu}{\partial\zeta}-\mathcal{B}\frac{\partial\mu}{\partial\eta}\right)-\mu\frac{\mathcal{B}^2+\mathcal{G}^2}{Re(\Delta\eta)^2} \end{aligned}$$

and

$$\begin{aligned} S(j) = \frac{St}{\Delta t}\omega_{i,j}^{k}+\Bigg\{ & -u\frac{\partial\omega}{\partial\zeta}+\frac{1}{Re}\Bigg[\mu\Big(\frac{\partial^2\omega}{\partial\zeta^2}-2\mathcal{B}\frac{\partial^2\omega}{\partial\zeta\partial\eta}\Big) \\ & +2\Big(\frac{\partial\mu}{\partial\zeta}-\mathcal{B}\frac{\partial\mu}{\partial\eta}\Big)\frac{\partial\omega}{\partial\zeta}+2\mathcal{G}\Big(\frac{\partial^2\mu}{\partial\zeta\partial\eta}-\mathcal{B}\frac{\partial^2\mu}{\partial\eta^2}\Big)\Big(\mathcal{G}\frac{\partial v}{\partial\eta}-\frac{\partial u}{\partial\zeta}+\mathcal{B}\frac{\partial u}{\partial\eta}\Big) \\ & +\Big[\frac{\partial^2\mu}{\partial\zeta^2}-2\mathcal{B}\frac{\partial^2\mu}{\partial\zeta\partial\eta}+\Big(\mathcal{B}^2-\mathcal{G}^2\Big)\frac{\partial^2\mu}{\partial\eta^2} \\ & -(\mathcal{A}-2\mathcal{B}\mathcal{H})\frac{\partial\mu}{\partial\eta}\Big]\Big(\mathcal{G}\frac{\partial u}{\partial\eta}+\frac{\partial v}{\partial\zeta}-\mathcal{B}\frac{\partial v}{\partial\eta}\Big)\Bigg]+\frac{Ha^2}{Re}\mathcal{G}\frac{\partial u}{\partial\eta}\Bigg\}_{i,j}^{k}. \end{aligned}$$

The heat transfer equation (27) is solved by using its discretized version

$$\theta_{i,j}^{k+1} = \theta_{i,j}^{k} + \frac{\Delta t}{St}\Bigg[- u\Big(\frac{\partial\theta}{\partial\zeta} - \mathcal{B}\frac{\partial\theta}{\partial\eta}\Big) - v\mathcal{G}\frac{\partial\theta}{\partial\eta} + \frac{1}{Pr\,Re}\Big\{\frac{\partial^2\theta}{\partial\zeta^2} - 2\mathcal{B}\frac{\partial^2\theta}{\partial\zeta\partial\eta} + (\mathcal{B}^2+\mathcal{G}^2)\frac{\partial^2\theta}{\partial\eta^2} - (\mathcal{A}-2\mathcal{B}\mathcal{H})\frac{\partial\theta}{\partial\eta}\Big\} + \frac{Ec}{Re}\mu\dot{\gamma}^2 + Ha^2 Ec\,u^2\Bigg]_{i,j}^{k}. \tag{34}$$

Updated temperature field is now employed in the mass transfer equation. The discretized form of the mass transfer equation (28) is

$$\begin{aligned} c_{i,j}^{k+1} = c_{i,j}^{k} + \frac{\Delta t}{St}\Bigg[& - u\Big(\frac{\partial c}{\partial\zeta} - \mathcal{B}\frac{\partial c}{\partial\eta}\Big) - v\mathcal{G}\frac{\partial c}{\partial\eta} \\ & + \frac{1}{Re\,Sc}\Big\{\frac{\partial^2 c}{\partial\zeta^2} - 2\mathcal{B}\frac{\partial^2 c}{\partial\zeta\partial\eta} + (\mathcal{B}^2+\mathcal{G}^2)\frac{\partial^2 c}{\partial\eta^2} - (\mathcal{A}-2\mathcal{B}\mathcal{H})\frac{\partial c}{\partial\eta}\Big\}\Bigg]_{i,j}^{k} \\ & + \Bigg[\frac{Sr}{Re}\Big\{\frac{\partial^2\theta}{\partial\zeta^2} - 2\mathcal{B}\frac{\partial^2\theta}{\partial\zeta\partial\eta} + (\mathcal{B}^2+\mathcal{G}^2)\frac{\partial^2\theta}{\partial\eta^2} - (\mathcal{A}-2\mathcal{B}\mathcal{H})\frac{\partial\theta}{\partial\eta}\Big\}\Bigg]_{i,j}^{k+1}. \end{aligned} \tag{35}$$

Dimensionless wall shear stress, Nusselt number [14] and Sherwood number [19], representing the local heat and mass flux to the arterial wall respectively, are computed by using the formulae

$$\tau_{\mathrm{w}} = -\left(\mu\frac{\partial u}{\partial y}\right)_{\mathrm{wall}}, \quad Nu = -\left(\frac{\partial\theta}{\partial y}\right)_{\mathrm{wall}} \quad \text{and} \quad Sh = -2\left(\frac{\partial c}{\partial y}\right)_{\mathrm{wall}}. \tag{36}$$

For a better insight into the heat and mass transport phenomenon in a pulsatile flow, time-averaged Nusselt number and Sherwood number are computed by using the formulae

$$TANu = \int_0^1 Nu\,dt \quad \text{and} \quad TASh = \int_0^1 Sh\,dt\,. \tag{37}$$

8 Stability Criteria of the Numerical Scheme

The time step Δt is selected through some restrictions on the fluid flow. The first restriction is the well-known CFL [20] condition. It states that the fluid can move through at most one cell in each time step, i.e.

$$\Delta t_1 \le \min\left[\frac{\Delta x}{|u|}, \frac{\Delta y}{|v|}\right]_{(i,j)}. \tag{38}$$

The viscous effect of the fluid gives the second restriction and is given by

$$\Delta t_2 \leq \min \left[\frac{Re}{2} \frac{\Delta x^2 \Delta y^2}{\Delta x^2 + \Delta y^2} \right]_{(i,j)} . \tag{39}$$

Finally, Δt is calculated by the relation

$$\Delta t = \beta \min \left[\Delta t_1, \, \Delta t_2 \right], \quad 0 < \beta < 1 . \tag{40}$$

9 Results and Discussion

Grid independence test has been performed by calculating the axial u-velocity and shown in Table 1. Obtained results for different grid sizes show that the result differs for grid-size 0.015×0.015 but almost same for other two grid sizes 0.010×0.010 and 0.005×0.005. Finally, the grid-size 0.010×0.010 is selected for further computations.

Table 1: Velocity (u) in steady flow of a Newtonian fluid in a long straight channel

Grid	Re	y	u	Exact value of u ($u = y - y^2$)
0.015×0.015	600	0.1	0.0911	0.09
		0.3	0.2152	0.21
		0.5	0.2584	0.25
0.010×0.010		0.1	0.0899	0.09
		0.3	0.2098	0.21
		0.5	0.2497	0.25
0.005×0.005		0.1	0.0899	0.09
		0.3	0.2097	0.21
		0.5	0.2497	0.25

To verify the present numerical scheme we have calculated the axial velocity for the steady flow of a Newtonian fluid in a long straight channel for $Re = 600$ and

Table 2: Results for axial velocity in steady flow of a Newtonian fluid in a long straight channel for $Re = 600$, $Ha = 0$

	$y = 0$	$y = 0.1$	$y = 0.3$	$y = 0.5$	$y = 0.7$	$y = 0.9$	$y = 1$	Scheme
$u = y - y^2$	0	0.09	0.21	0.25	0.21	0.09	0	Exact
u	0	0.0899	0.2099	0.2499	0.2099	0.0899	0	Midya et al. [7]
u	0	0.0899	0.2098	0.2497	0.2098	0.0899	0	Present

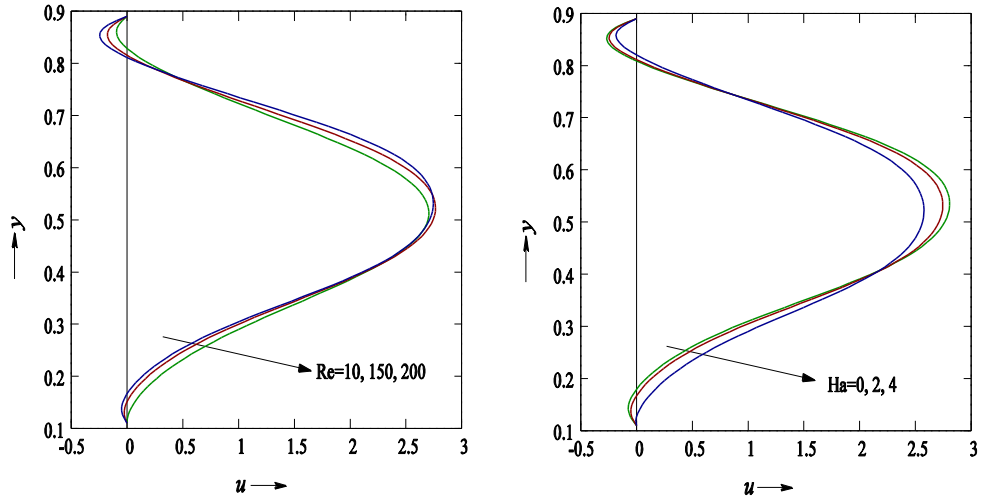

(a) (b)

Fig. 3: Axial velocity profile at $x = 4$ for: (a) various Re, $St = 0.1$, $Ha = 2$; and (b) various Ha, $St = 0.1$, $Re = 200$.

compared the result with the result obtained by Layek and Midya [7] and are presented in Table 2. An excellent agreement is found which confirms the accuracy of our numerical code.

At the very beginning of our discussion, to demonstrate the effects of Reynolds number and Hartmann number on the axial velocity profile, Figs. 3 (a) and (b) are presented. Axial velocity is maximum near the channel axis and decreases towards both the walls. Fluid flow becomes reversed near both walls and formation of vortices are noted. Intensity of back flow is stronger near the upper wall compared to the lower wall. Back flow velocity gets enhanced with increasing Reynolds number (Fig. 3 (a)). However, this flow reversal phenomenon could be reduced by increasing the intensity of the externally imposed magnetic field (Fig. 3 (b)).

Next we shall focus our attention to investigate the effect of the magnetic field on the peak shear stress at both walls. Peak value of shear stress at systolic peak flow time (Fig. 4) is noted near the throat of the stenosis for both walls. Peak shear stress at lower wall has larger magnitude than that at upper wall. Peak shear stress increases with the intensity of the applied magnetic field at both walls.

Figures 5 (a) and (b) represent the distributions of wall pressure along the lower and upper walls respectively at the systolic peak flow time. A rapid fall in wall pressure occurs near the constricted region of the channel. Such a phenomenon produces a health risk. The arterial wall may collapse in this region due to the sudden fall in

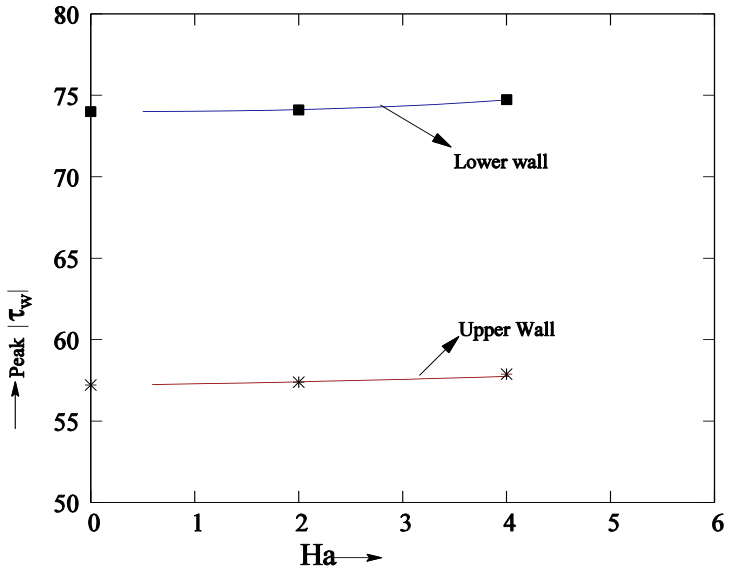

Fig. 4: Variation of peak wall shear stress with Hartmann number.

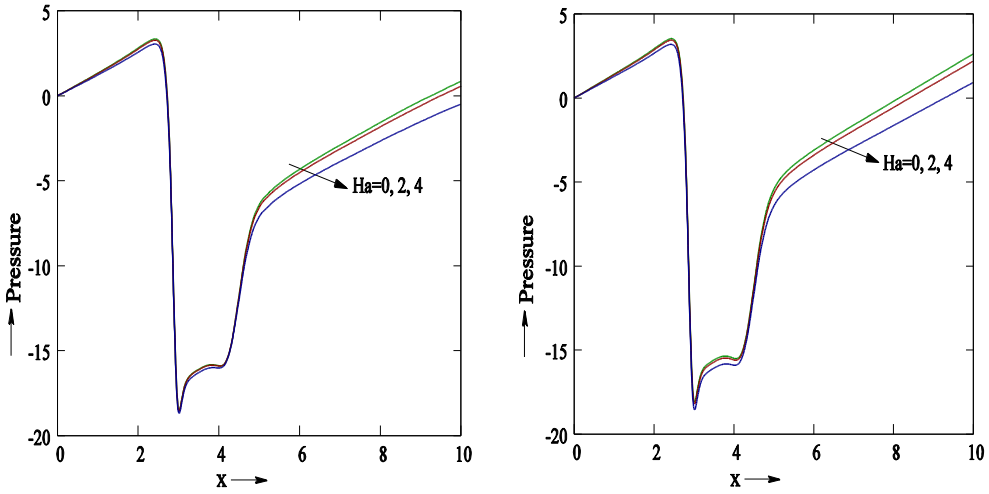

Fig. 5: Distribution of wall pressure along: (a) lower wall; and (b) upper wall for various Ha and $St = 0.1$, $Re = 200$.

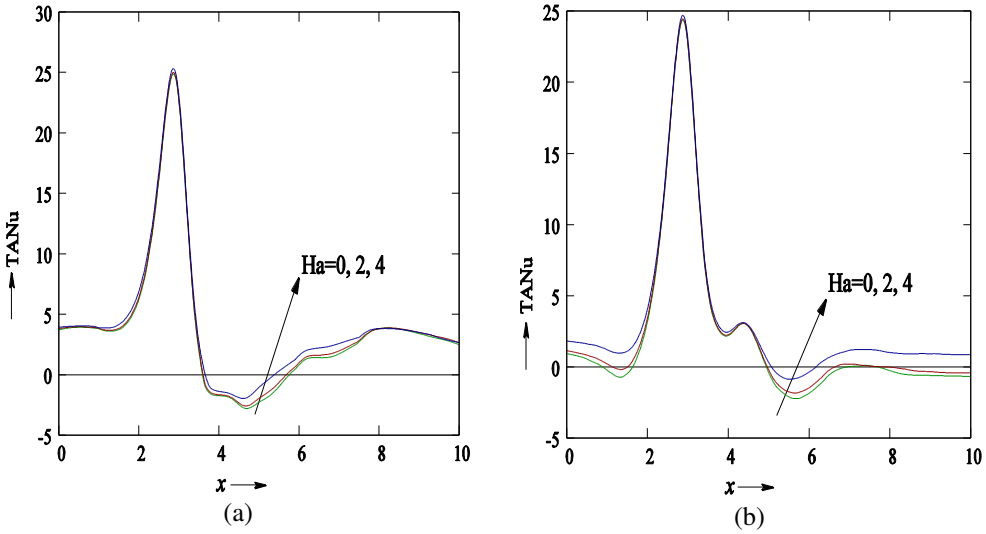

Fig. 6: Distribution of time averaged Nusselt number along: (a) lower wall; and (b) upper wall for various Ha and $St = 0.1$, $Re = 200$, $Pr = 21$, $Ec = 0.0002$.

wall pressure [21]. Wall pressure falls further along the lower wall than the upper wall. Increasing Hartmann number causes further fall in wall pressure along the both walls.

Our next interest is to study the effect of the magnetic field on the heat transfer phenomenon at both walls of the channel by investigating the distribution of time averaged Nusselt number. For this Figs. 6 (a) and (b) are presented for the variations of Ha. At each wall it is observed that the heat transfer rate rises significantly at the constricted portion of the channel and attains a maximum value near the throat. More heat transfer takes place at the lower wall compared with the upper wall. It is found that increasing intensity of the magnetic field increases the heat transfer rate. These results agree well with Majee and Shit [16] and Tashtoush and Magableh [22]. In some regions at the downstream side (for upper wall at upstream side also) of the constriction, time averaged Nusselt number becomes negative. Thus in these regions heat transfer takes place in reverse direction in most of the time of the cardiac cycle indicating that the fluid's temperature falls below the wall temperature in these regions.

Mass transportation from the blood stream into the arterial wall is measured with the help of Sherwood number. For a better understanding of the mass transfer phenomenon for a pulsatile flow in a constricted channel and to investigate the effect of applied magnetic field on it, distribution of the time-averaged Sherwood num-

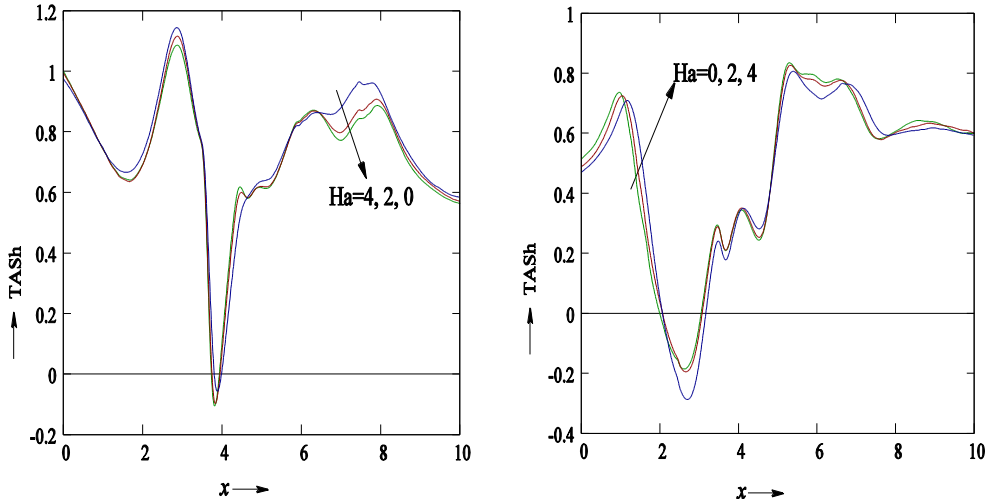

Fig. 7: Distribution of time averaged Sherwood number along: (a) lower wall; and (b) upper wall for various Ha and $St = 0.1$, $Re = 200$, $Sc = 3$, $Sr = 0.4$.

ber along both wall are computed for several Hartmann number and depicted in Figs. 7 (a) and (b). Rate of mass transfer along the lower wall increases with increasing Hartmann number and maximum mass transfer rate noted near the throat. Several peaks exist in the downstream side indicating the possibility for formation of several stenotic lesions. However at the upper wall mass transfer in reverse direction is found in some region around the stenotic throat and increased mass transfer rate is observed at both the fore and aft side of the constriction.

For a better insight into the flow field, pattern of streamlines at $t = 0.18$ are presented in Figs. 8 (a)–(c) for various Hartmann numbers. Two flow separation zones are seen in the downstream vicinity of the constriction at both walls. Strength

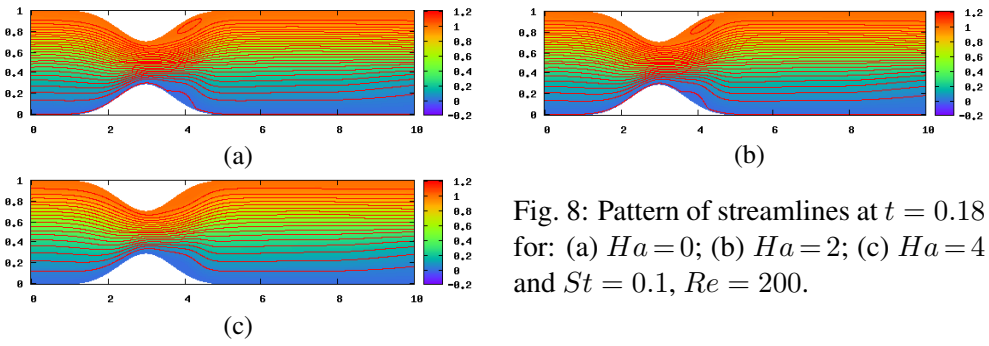

Fig. 8: Pattern of streamlines at $t = 0.18$ for: (a) $Ha = 0$; (b) $Ha = 2$; (c) $Ha = 4$ and $St = 0.1$, $Re = 200$.

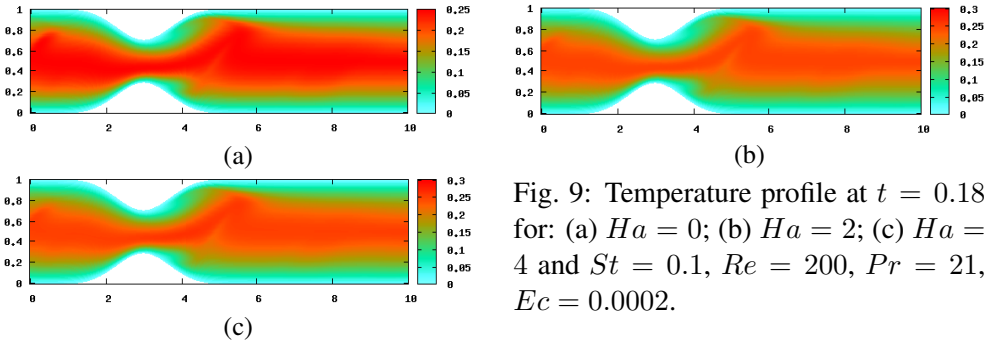

(a) (b) (c)

Fig. 9: Temperature profile at $t = 0.18$ for: (a) $Ha = 0$; (b) $Ha = 2$; (c) $Ha = 4$ and $St = 0.1$, $Re = 200$, $Pr = 21$, $Ec = 0.0002$.

of vortex formed at the upper wall is stronger than that at the lower wall. It is found that the vortices gradually disappear with increasing Hartmann number. Thus suitable strength of magnetic field may be applied to prevent or delay the flow separation.

Temperature profile of the fluid at the systolic peak flow time for various Hartmann number are reflected through Figs. 9 (a)–(c). Applied magnetic field produces heat which rises the temperature of the fluid. Thus with increasing Hartmann number, fluid's temperature gets enhanced from the central region to the boundaries. Production of heat with increasing intensity of the magnetic field increases the rate of heat transfer at the channel walls.

Figures 10 (a)–(c) and Figs. 11 (a)–(c) are prepared to exhibit the concentration profile of the fluid at the systolic peak flow time for various Hartmann number and Soret number respectively. Mass concentration of the fluid gets dispersed from the axial region to the boundaries with increasing Hartmann or Soret number and increases the mass transfer rate at the channel walls. At the lower wall concentration scatters more in the downstream side, but for the upper wall it happens for both upstream and downstream side of the constriction. Thus formation of a stenosis in a

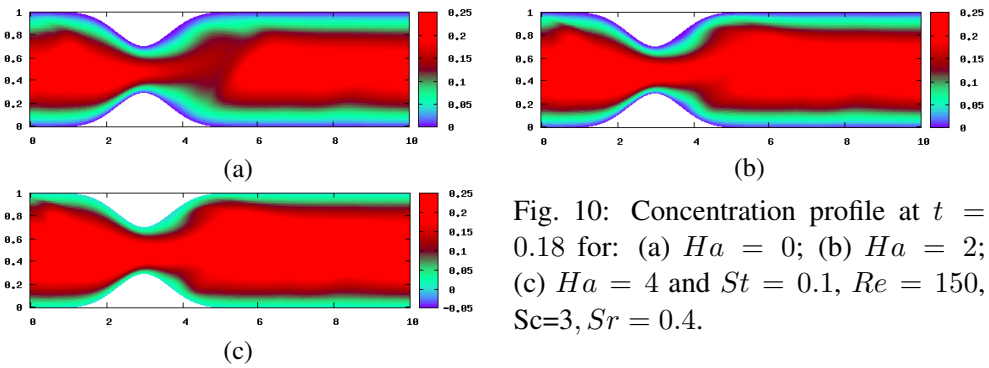

(a) (b) (c)

Fig. 10: Concentration profile at $t = 0.18$ for: (a) $Ha = 0$; (b) $Ha = 2$; (c) $Ha = 4$ and $St = 0.1$, $Re = 150$, Sc=3, $Sr = 0.4$.

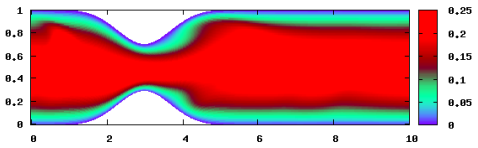

(a)

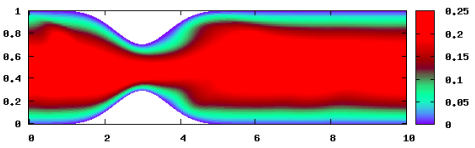

(b)

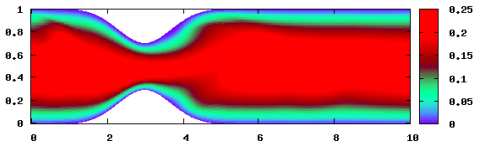

(c)

Fig. 11: Concentration profile at $t = 0.18$ for: (a) $Sr = 0$; (b) $Sr = 0.2$; (c) $Sr = 0.4$ and $St = 0.1$, $Re = 150$, $Ha = 2$, $Sc = 3$.

blood vessel further influence in the development of the disease and increase in Hartmann and Soret number may worsen the situation.

10 Conclusion

Computational results for the MHD pulsatile flow of a non-Newtonian electrically conducting fluid in a two-dimensional constricted channel have been obtained in the present investigation. The governing non-linear equations of motion together with the equations of heat and mass transfer have been solved numerically under the MHD framework. The study reveals that the applied magnetic field has prominent effect on the flow field and heat and mass transfer phenomenon. Main findings of this investigation could be summarized as follows:

- The flow field is asymmetric for Reynolds number (≥ 150) taken in this study.
- Applied magnetic field increases the peak wall shear stress at both walls.
- Flow separation could be prevented or delayed with the application of suitable strength of magnetic field.
- Increasing Hartmann number enhances the rate of heat transfer at both walls.
- Applied magnetic field increases the rate of mass transfer at channel walls.
- External magnetic field may promote the development of atherosclerosis.

The authors state that there is no conflict of interest.

REFERENCES

[1] J.C. MISHRA, S.D. ADHIKARY (2016) MHD oscillatory channel flow, heat and mass transfer in a physiological fluid in presence of chemical reaction. *AAlexandria Engineering Journal* **55** 287-297.

[2] J. SASIKUMAR, R. GAYATHRI, A. DOVINDARAJAN (2018) Heat and mass transfer effects on MHD oscillatory flow of a couple stress fluid in an asymmetric tapered channel. *IOP Conference Series: Materials Science and Engineering* **402** 012167.

[3] A. ALI, H. FAROOQ, Z. ABBAS, Z. BUKHARI, ATTIA FATIMA (2020) Impact of Lorentz force on the pulsatile flow of a non-Newtonian Casson fluid in a constricted channel using Darcy's law: a numerical study. *Scientific Reports* **10** 10629.

[4] G.C. LAYEK, M.S. MANDAL, H.A. KHALAF (2014) Bifurcation phenomena and control for magnetohydrodynamic flows in a smooth expanded channel. *Chinese Physics B* **23** 114701.

[5] M. GAD-EL-HAK, D.M. BUSHNELL (1991) Separation control: Review. *ASME Journal of Fluids Engineering* **113** 5-30.

[6] A. ALI, M. UMAR, Z. ABBAS, G. SHAHZADI, Z. BUKHARI, A. SALEEM (2021) Numerical investigation of MHD pulsatile flow of micropolar fluid in a channel with symmetrically constricted walls. *Mathematics* **9** 1000.

[7] C. MIDYA, G.C. LAYEK, A.S. GUPTA, T.R. MAHAPATRA (2003) Magnetohydrodynamics viscous flow separation in a channel with constrictions. *ASME Journal of Fluids Engineering***125** 952-962.

[8] G.C. LAYEK, C. MIDYA (2007) Control of flow separation in a channel with step using eletro-magnetic force. *Magnetohydrodynamics* **43**(1) 3-14.

[9] V.P. RATHOD, S. TANVEER, I.S. RANI, G.G. RAJPUT (2006) Pulsatile flow of blood with periodic body acceleration and magnetic field through an exponentially diverging vessel. *Journal of Ultra Scientist of Physical Sciences*. **18** 417-426.

[10] N. NANDAKUMAR, K.C. SAHU, M. ANAND (2015) Pulsatile flow of a shear-thinning model for blood through a two-dimensional stenosed channel. *European Journal of Mechanics B/Fluids* **49** 29-35.

[11] S. BANDYOPADHYAY, G.C. LAYEK (2012) Study of magnetohydrodynamic pulsatile flow in a constricted channel. *Communications in Nonlinear Science and Numerical Simulation* **17**(6) 2434-2446.

[12] Y.I. CHO, K.R. KENSEY (1991) Effects of the non-Newtonian viscosity of blood on flows in a diseased arterial vessel. Part I: Steady flows. *Biorheology* **28** 241-262.

[13] J.L. BANSAL (1992) "Viscous Fluid Dynamics". Oxford & IBH Publishing Company.

[14] G.C. SHIT, S. MAJEE (2018) Magnetic field interaction with blood flow and heat transfer through diseased artery having Abdominal Aortic Aneurysm. *European Journal of Mechanics - B/Fluids* **71** 1-14.

[15] H. VAIDYA, C. RAJASHEKHAR, G. MANJUNATHA, K.V. PRASAD, O.D. MAKINDE, K. VAJRAVELU (2020) Heat and mass transfer analysis of MHD peristaltic flow through a complaint porous channel with variable thermal conductivity. *Physica Scripta* **95** 045219.

[16] S. MAJEE, G.C. SHIT (2017) Numerical investigation of MHD flow of blood and heat transfer in a stenosed arterial segment. *Journal of Magnetism and Magnetic Materials* **424** 137-147.

[17] G. PEDRIZZETTI (1996) Unsteady tube flow over an expansion. *Journal of Fluid Mechanics* **310** 89-111.

[18] P. NIYOGI (2006) "Introduction to Computational Fluid Dynamics". Pearson Education India.

[19] J.R. ZIERENBERG, H. FUJIOKA, V. SURESH, R.H. BARTLETT, R.B. HIRSCHL, J.B. GROTBERG (2006) Pulsatile flow and mass transport past a circular cylinder. *Physics of Fluid* **18** 013102.

[20] R. COURANT, K. FRIEDRICHS, H. LEWY (1928) On the Partial Difference Equations of Mathematical Physics. *Mathematische Annalen* 10032-74.

[21] D. TANG, C. YANG, S. KOBAYASHI, D.N. KU (2001) Generalized finite difference method for 3-D viscous flow in stenotic tubes with large wall deformation and collapse. *Applied Numerical Mathematics* **38** 49.

[22] B. TASHTOUSH, A. MAGABLEH (2008) Magnetic field effect on heat transfer and fluid flow characteristics of blood flow in multi-stenosis arteries. *Heat Mass Transfer* **44** 297-304.